Check for updates

Spectroscopic fingerprint of charge order melting driven by quantum fluctuations in a cuprate

W. S. Lee [1 ✉], Ke-Jin Zhou [2 ✉], M. Hepting [1], J. Li[2], A. Nag[2], A. C. Walters[2], M. Garcia-Fernandez[2], H. C. Robarts[2], M. Hashimoto[3], H. Lu[4], B. Nosarzewski[4], D. Song[5], H. Eisaki[5], Z. X. Shen [1,6], B. Moritz [1], J. Zaanen[7] and T. P. Devereaux [1,6 ✉]

Copper oxide high-T_C superconductors possess a number of exotic orders that coexist with or are proximal to superconductivity. Quantum fluctuations associated with these orders may account for the unusual characteristics of the normal state, and possibly affect the superconductivity[1-4]. Yet, spectroscopic evidence for such quantum fluctuations remains elusive. Here, we use resonant inelastic X-ray scattering to reveal spectroscopic evidence of fluctuations associated with a charge order[5-14] in nearly optimally doped $Bi_2Sr_2CaCu_2O_{8+\delta}$. In the superconducting state, while the quasielastic charge order signal decreases with temperature, the interplay between charge order fluctuations and bond-stretching phonons in the form of a Fano-like interference increases, an observation that is incompatible with expectations for competing orders. Invoking general principles, we argue that this behaviour reflects the properties of a dissipative system near an order–disorder quantum critical point, where the dissipation varies with the opening of the pseudogap and superconducting gap at low temperatures, leading to the proliferation of quantum critical fluctuations, which melt charge order.

Charge order (CO), which is ubiquitous in hole-doped cuprates[5-14], is accompanied by a negligible lattice deformation (approximately 0.1 pm, ref. [15]); however, signatures of valence electron density modulations due to CO can be detected by resonant inelastic X-ray scattering (RIXS) at the Cu L edge. RIXS resolves both the quasistatic and dynamical inelastic signals[8,16], as highlighted in Fig. 1a, particularly the intensity of the inelastic branch of excitations below 0.1 eV. These excitations possess an energy scale similar to that of bond-stretching phonons, which exhibit anomalous softening and broadening in certain portions of reciprocal space, observed using inelastic neutron scattering and non-resonant inelastic X-ray scattering[17,18]. These behaviours have suggested a coupling with CO[17,18] and possibly some form of charge collective mode[19]. However, while neutron and non-resonant X-ray scattering measure the phonon self-energy (meaning the dynamical structure factor), RIXS largely reflects the electron–phonon coupling itself and its interplay with charge excitations[16,20]. With superb momentum resolution, RIXS at the Cu L edge has already revealed two distinct anomalies associated with CO excitations due to a Fano-like interference effect[16], as shown in Fig. 1b: (1) an apparent softening of the RIXS phonon at the CO wave-vector (Q_{CO}), and (2) creation of a 'funnel'-like spectral weight emanating from Q_{CO} with a non-monotonic integrated momentum distribution whose maximum occurs at $Q > Q_{co}$.

Figure 1c shows the temperature evolution of CO in the quasielastic region (Methods, and Extended Data Figs. 1 and 2) with corresponding energy-integrated CO peak profiles in Fig. 1d. A broad peak centred at approximately 0.25 reciprocal lattice units (r.l.u.) already exists at 260 K, essentially T^*, the pseudogap temperature[21]. As the temperature decreases, the CO peak height gradually increases and the width narrows (Fig. 1e), consistent with an increase in both the amplitude and correlation length of the order parameter. The CO peak height reaches a maximum at T_C and then decreases precipitously upon entering the superconducting state (becoming less than one-third of the value at 90 K), but with a correlation length of roughly 30 Å at 15 K. These observations are consistent with temperature evolution of CO in $YBa_2Cu_3O_{6+x}$[8,9] and near-optimally doped $La_{1-x}Sr_xCuO_4$[14,15], where reduction of CO for $T < T_C$ was interpreted in terms of order parameter competition with superconductivity.

A very different story emerges from the higher-energy inelastic response, as shown in the raw data of Fig. 2a. Upon cooling from 260 K, the RIXS phonon dispersion gradually softens roughly centred around Q_{CO}, from approximately 0.2 to 0.35 r.l.u. (Fig. 2b). Below the superconducting transition temperature T_C, this softening becomes more pronounced and a dip in the dispersion develops at Q_{CO} (Fig. 2b), in contrast to the substantial reduction in quasielastic CO (Fig. 1 and Fig. 2a). Between 260 K and 15 K, the RIXS phonon peak energy at Q_{CO} shifts from 58 meV to 36 meV (inset of Fig. 2b). This shift is evident even in the raw data without applying any fitting (Fig. 2c). Both the funnel-like spectral weight (Fig. 2d) and integrated momentum-distribution curve for the phonon intensity (Fig. 2e) exhibit substantial enhancement once the system enters the superconducting state.

These behaviours are different from the phonon self-energy evolution in the superconducting state probed by non-resonant inelastic X-ray and neutron scattering. The opening of a superconducting gap in the particle–hole continuum (here $2\Delta \approx 80$ meV; ref. [21]) should sharpen the bond-stretching phonon spectral width, as its energy scale lies below 2Δ (ref. [22]); however, the RIXS phonon width near Q_{CO} broadens, with no obvious changes discernible elsewhere (Fig. 2f). Neither can they be explained by a Kohn anomaly, which would require unrealistically large electron–phonon coupling strength to produce the observed magnitude of softening.

[1]Stanford Institute for Materials and Energy Sciences, SLAC National Accelerator Laboratory and Stanford University, Menlo Park, CA, USA. [2]Diamond Light Source, Harwell Campus, Didcot, UK. [3]Stanford Synchrotron Radiation Lightsource, SLAC National Accelerator Laboratory, Menlo Park, CA, USA. [4]Department of Physics, Stanford University, Stanford, CA, USA. [5]National Institute of Advanced Industrial Science and Technology (AIST), Tsukuba, Japan. [6]Geballe Laboratory for Advanced Materials, Departments of Physics and Applied Physics, Stanford University, Stanford, CA, USA. [7]Instituut-Lorentz for Theoretical Physics, Leiden University, Leiden, The Netherlands. ✉e-mail: leews@stanford.edu; kejin.zhou@diamond.ac.uk; tpd@stanford.edu
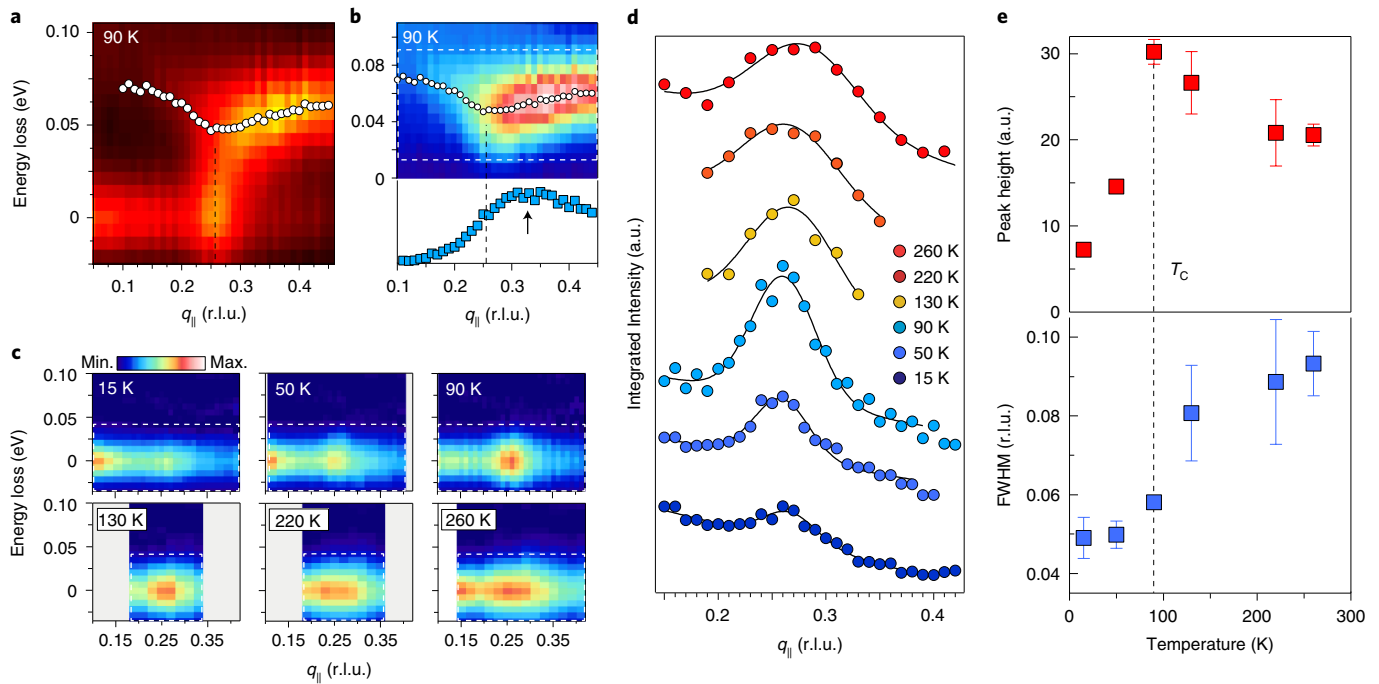
Fig. 1 | Temperature dependence of the CO in the quasielastic region. a, Raw RIXS intensity map along the $(0,0)–(1,0)$ direction taken at T_C (90 K). White markers indicate the fitted peak positions of the excitations that possess an energy scale similar to that of bond-stretching phonons. The black dashed line indicates $\mathbf{Q}_{CO}$. **b**, Top: RIXS phonon map obtained by subtracting the fitted elastic peak from raw data. Bottom: momentum-distribution curve of integrated phonon intensity within the white dashed box in the top panel. The dashed line and arrow indicate $\mathbf{Q}_{CO}$ and the maximum of the curve, respectively. **c**, Quasielastic maps taken at different temperatures obtained by subtracting the fitted phonon and background from raw data (Fig. 2a). **d**, CDW peak profiles obtained by integrating the quasielastic maps within the white dashed boxes in **c**. The black curves are fits to CDW peak profiles using a Gaussian function plus a linear background. a.u., arbitrary units. **e**, Fitted intensity (top) and FWHM (bottom) of CDW peak profiles at different temperatures. The error bars are the s.d. of the fit except for the 130-K and 220-K data, whose error bars were estimated via the uncertainty of the linear background.

In addition, the Kohn anomaly should decrease concomitant to the reduction in CO magnitude, as seen in the low-energy phonon anomalies in yttrium barium copper oxide via IXS[23,24]. These again testify to the fact that the RIXS phonon cross-section is reflective of not the phonon self-energy, but rather the electron–phonon coupling itself and its interplay with underlying charge excitations[16,20]. Thus, the enhancement of the RIXS phonon anomalies near $\mathbf{Q}_{CO}$ should be attributed to an increase in spectral weight associated with inelastic CO excitations in the superconducting state. Yet, the contrasting temperature evolution shown in Figs. 1 and 2 reveals a major paradox, which departs from the picture of order parameter competition as in Landau theory, where the reduction of CO due to superconductivity ultimately would lead to a weakening of the CO excitations' spectral weight, in contrast with our observations.

We propose a natural way to understand this temperature dependence. Due to a much smaller mass for electrons than that of atoms forming solids, an electronic crystal, such as the CO, can be subjected to severe quantum zero-point motion that can reduce the magnitude of the order. The fact that the weight of the CO excitations at the elevated energies of the bond-stretching phonon decouples from the magnitude of the static order parameter may signal that the system lies in close proximity to a strong-coupling, order–disorder, phase-driven quantum phase transition, rather than one driven by amplitude fluctuations[25]. This is analogous to dynamical stripes, which were based on a similar organization of the spin excitations measured by inelastic neutron scattering[26,27] in the La family of cuprate superconductors. Figure 3 shows a sketch of the evolution of a CO and the associated excitations (vertical panels) when approaching the quantum critical point (QCP, $g_c(\alpha)$) via changing a conceptual tuning parameter g and 'dissipation' α.

In an isolated quantum system (where there is no dissipation, so $\alpha = 0$) with a g value far away from g_c on the ordered side (denoted renormalized classical, RC) of the phase transition, excitations can be characterized by (1) a static order parameter, (2) the associated Goldstone bosons and (3) a branch-cut continuum associated with quantum fluctuations of the quantum critical state (red shading in Fig. 3), starting at energy $\omega \sim kT_0$ and extending to high energy (T_0 denotes the transition temperature in the RC region). Note that in a commensurate CO system the zero-energy Goldstone modes will acquire a pinning gap. We assume that this gap, if present, is substantially smaller than the bond-stretching phonon energy and the energy resolution of our RIXS instrument. At the QCP, both the static order and Goldstone bosons vanish, with spectral weight transferred into the continuum.

In practice, this should be a dissipative quantum phase transition[28]. The CO quantum fluctuations inevitably couple to the electrons near the Fermi surface that dissipate the order parameter quantum fluctuations via the creation of particle–hole excitations. It is well documented that the coupling to a heat bath generically suppresses quantum fluctuations. A famous example is the Caldeira–Leggett problem of a tunnelling particle that comes to a standstill when the coupling to the heat bath exceeds a critical strength[29]. In fact, the present situation is very close to the problem of a network of resistively shunted Josephson junctions approaching the superconductor–insulator quantum phase transition. The (Euclidean) path integral offers a simple explanation: the heat bath effectively induces long-range interactions along the time direction that stiffen the temporal fluctuations, driving the system away from the QCP.[30]

Here, the dissipation should be strongly temperature dependent. The opening of the pseudogap below T^* and a clean gap (2Δ) in
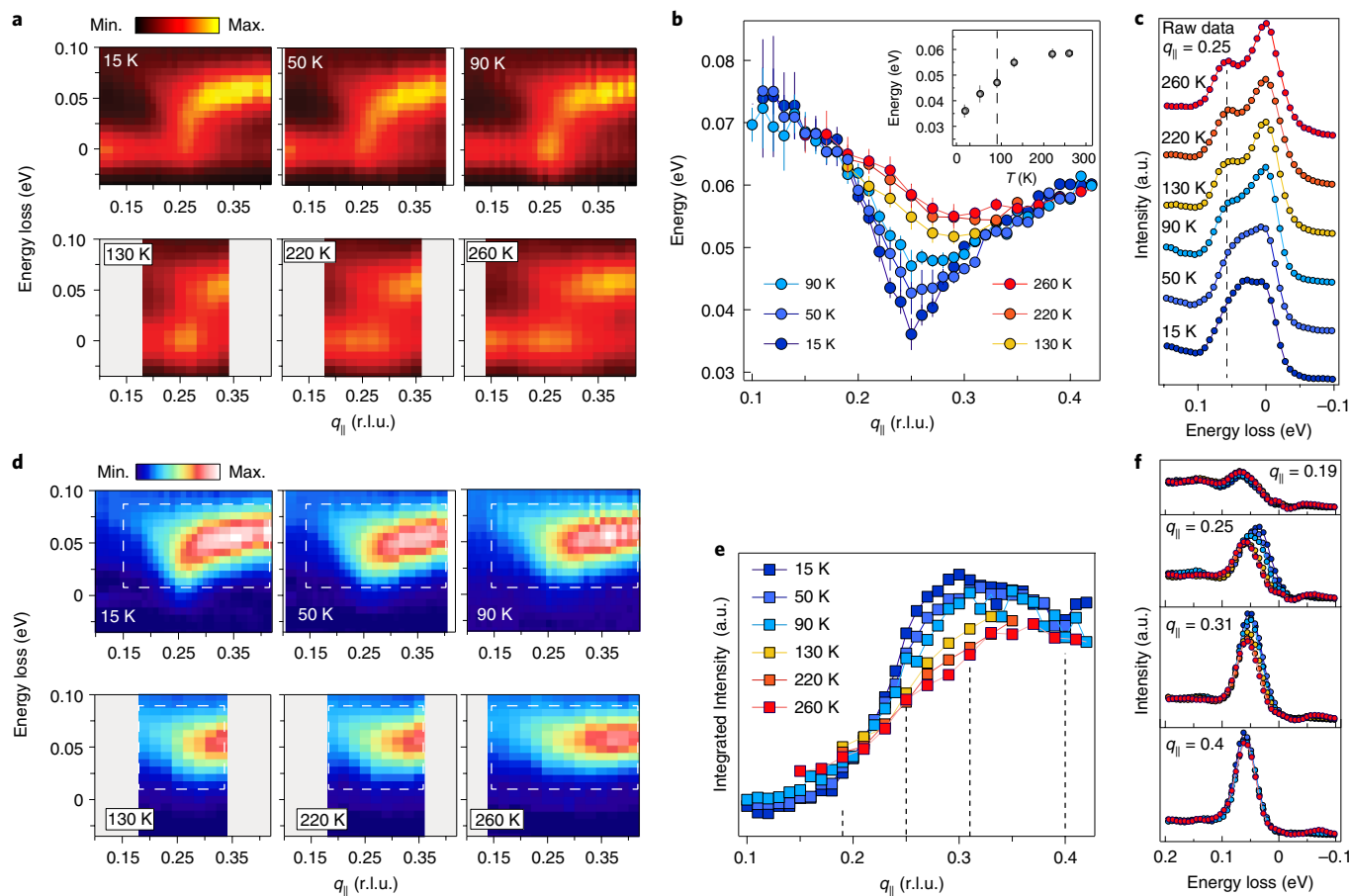
Fig. 2 | The temperature dependence of RIXS phonon spectra. a, Raw RIXS intensity maps taken at different temperatures. **b**, Fitted RIXS phonon dispersions at different temperatures. Inset: the phonon energy at in-plane projected momentum transfer $q_{\parallel} = 0.25$ r.l.u. The dashed line indicates the superconducting transition temperature (T_C). The error bars are estimated using the 95% confidence interval of the fit. **c**, Raw energy-loss spectrum at ~$\mathbf{Q}_{CO}$ at different temperatures. The vertical dashed line indicates the phonon peak position at 260 K, serving as a guide to the eye for the shift of position at low temperatures. **d**, RIXS phonon maps obtained by subtracting the fit of the elastic peaks from the raw data. **e**, Integrated momentum-distribution curves at different temperatures, obtained by integrating RIXS phonon maps within the white dashed boxes indicated in **d**. **f**, Temperature evolution of RIXS phonon spectra at representative $q_{\parallel}$, as indicated by dashed lines in **e**.

the superconducting state will suppress the coupling to the particle–hole excitations below the gap. This substantially reduces dissipation at low temperatures, thereby enhancing the order parameter quantum fluctuations. We are unaware of explicit calculations dealing with this motif, as a fixed dissipation parameter at zero temperature is usually considered. However, it is easy to see the qualitative outcome (Fig. 3). At a given temperature, one can freeze α and compute the distance from $g_c(\alpha)$. Keeping the coupling constant fixed at g_1 and decreasing the dissipation parameter, the fluctuations would

be restored due to reduced damping, effectively pushing the system toward the QCP. In the context of our experimental observations, entering the superconducting state suppresses dissipation such that quantum fluctuations become more severe than those at higher temperatures and melt the CO.

We can model the resulting RIXS spectrum as a superposition between a discrete dispersive mode (bond-stretching phonon) and a continuum of quantum fluctuations emanating from $\mathbf{Q}_{CO}$. As is

Fig. 3 | Dissipation and QCP. A sketch of the evolution of a CO and the associated excitations (vertical panels) when approaching the QCP at $g_c(\alpha)$ via changing g at zero dissipation (grey panels) or varying dissipation at g_1 near g_c (light-red panels). The ordered side of the phase diagram is yellow shaded (RC), while the disordered side is blue shaded (quantum disordered, QD). The round red shading represents the static order at $\omega = 0$ and $\mathbf{q} = \mathbf{Q}_0$, whose intensity represents the magnitude of the order parameter. The red shaded area in $\omega > 0$ represents the branch-cut continuum of quantum fluctuations associated with the order. The purple lines represent the Goldstone mode associated with the order. Note that in a commensurate CO system the zero-energy Goldstone modes will acquire a pinning gap. The graininess of the continuum at higher dissipation illustrates its suppression from larger dissipation.
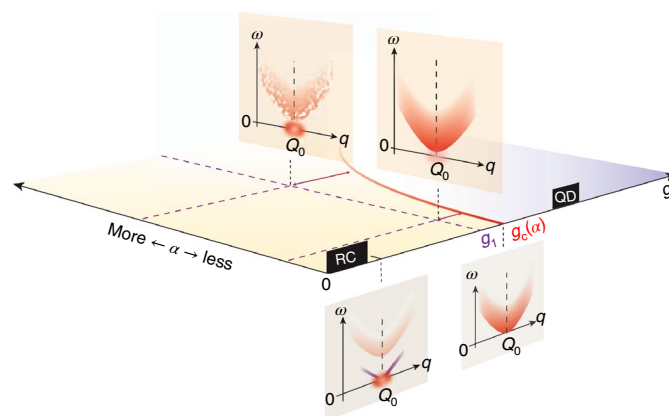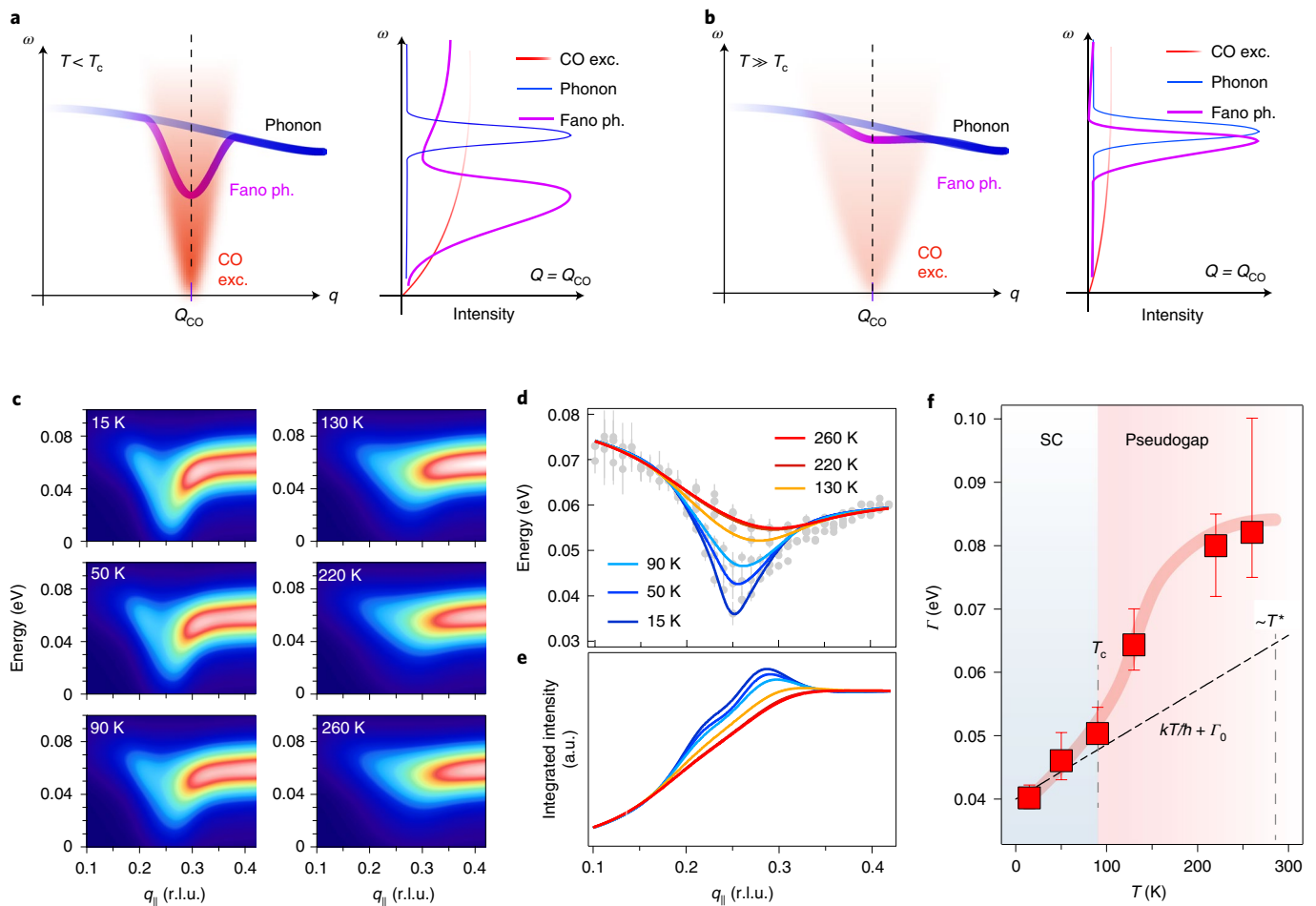
Fig. 4 | Modelling the Fano interference between CO excitations and bond-stretching phonons. a, Left: a sketch of the model to mimic the situation when $T < T_C$. The momentum dependence of the electron–bond-stretching phonon coupling strength is illustrated by the blue colour gradient along the phonon dispersion curve. The CO excitation continuum (CO exc.) is illustrated by the red shaded area. The dispersion modified by Fano interference with CO excitation is sketched as the purple curve (Fano ph.). Right: the Fano spectrum at $\mathbf{Q} = \mathbf{Q}_{CO}$. **b**, A sketch of the model and Fano spectra for $T \gg T_C$, where the CO is more damped in energy and broadened in momentum space, resulting a weaker Fano effect. **c**, Calculated phonon intensity maps for different temperatures. A Gaussian convolution of 35-meV FWHM is applied to account for the energy broadening due to instrument resolution in the experiment data. **d**, The peak positions of the Fano spectra shown in **c**. Grey symbols are the experimental data of Fig. 2b. **e**, Integrated momentum-distribution curves at different temperatures, obtained by integrating the maps shown in **c** from 0.01 to 0.09 eV. **f**, Γ at different temperatures. The vertical dashed lines indicate T_C and T^*. The black dashed line indicates $kT/\hbar$ plus $\Gamma_0 = 0.04$ eV. SC, superconductivity. The error bars were estimated from the range of Γ that can produce Fano phonon spectra at $\mathbf{Q}_{CO}$ with a peak energy within the error bars of the data at the same momentum position (grey markers and the error bars at 0.25 r.l.u. in **d**).

well known from Raman scattering, the coupling between a discrete mode and a continuum can lead to a distortion of the combined spectra, resulting in a Fano-like lineshape. This occurs where the phonon branch intersects the continuum near $\mathbf{Q}_{CO}$. The spectra can be modelled remarkably well using this simple and natural construction, where we take linearly dispersing electronic modes with fixed spectral weight, attenuated by a temperature-dependent damping constant. Their propagator takes the form of an anti-Lorentzian as a function of ω and momentum $\mathbf{q}$

$$\chi_\lambda(\mathbf{q}, \omega) = \frac{1}{\omega - \Omega_\mathbf{q}(\mathbf{q}) + i\Gamma(T)} - \frac{1}{\omega + \Omega_\mathbf{q}(\mathbf{q}) + i\Gamma(T)}$$

where $\Omega_\mathbf{q}(\mathbf{q}) = c|\mathbf{q} - \mathbf{Q}_{CO}|$ is the CO excitation energy at $\mathbf{q}$, c is the mode velocity and $\Gamma(T)$ is the damping, similar to the standard form for quantum critical excitations. To account for the effect of the finite CO correlation length on the continuum, we apply a Gaussian momentum broadening on $\chi_\lambda(\mathbf{q}, \omega)$, whose full-width at

half-maximum (FWHM) corresponds to the CO width shown in Fig. 1e (Methods). The Fano effect explains the CO-induced anomalies in the RIXS phonon cross-section (for example Fig. 4a,b), where the coupling reorganizes spectral weight according to the strength of the continuum. Note that the apparent Fano phonon (meaning the RIXS phonon) dispersion can substantially deviate from the actual phonon dispersion due to only the phonon self-energy in the momentum region where the Fano interference is strong. By adjusting only $\Gamma(T)$ (Methods and Extended Data Fig. 3), we can achieve excellent agreement with our temperature-dependent data, including the energy–momentum intensity map (Fig. 4c), phonon dispersion (Fig. 4d) and integrated phonon intensity momentum-distribution curve (Fig. 4e). From the fit, as the temperature decreases, the damping decreases, and appears to do so more rapidly when approaching T_C (Fig. 4f), presumably due to the opening of the superconductivity gap.

Interestingly, the increment of $\Gamma(T)$ is of the same order of magnitude as the Planckian dissipation[4], $kT/\hbar$, consistent with our

conjecture of dealing with strongly interacting quantum criticality[25]. We note that the zero-temperature residue $\Gamma_0 \approx 40\,$meV may be related to a disorder pinning gap or the effective gap in the quantum critical spectra, which are beyond the resolution of our current data. Higher-resolution RIXS spectra would allow us to gain further insight into the lower-energy structure of the electronic continuum.

Our results provide support for the existence of quantum phase fluctuations inside the superconducting dome, with the corresponding CO QCP located near the optimal doping in our Bi-2212 sample. Furthermore, our proposed dissipation-driven quantum melting of CO provides a fresh perspective on the relationship between CO and superconductivity, which is beyond a simple competition. It may provide a natural explanation for the lack of CO reduction inside the superconducting state of some other cuprates. Experiments on single-layer Bi-based cuprates (Bi-2201, ref. [10]) and underdoped $La_{2-x}Sr_xCuO_4$ (ref. [14]) tend to show CO largely insensitive to superconductivity. This lack of quantum melting of CO implies that proximity to the CO QCP may be material dependent; for some materials, the QCP even may lie beyond the superconducting dome[31]. In stripe-ordered $La_{2-x}Ba_xCuO_4$, signatures of charge density wave (CDW) excitations were also reported in underdoped compounds[32,33], and attributed to phase modes[32]. We argue that $La_{2-x}Ba_xCuO_4$ near $x = 1/8$ probably sits in the RC regime of Fig. 3, since the associated CO is more robust and heavily suppresses superconductivity around this doping level. Taken together with the coexisting spin order, it would be of great interest to identify signatures of all these modes as functions of doping and temperature. Finally, a broad CO feature still exists at T^*[34], and the excitations already play a role at high temperatures, where we find the pseudogap and strange metal behaviour[1]. So, it may well be that the pseudogap and the strange metal behaviours are intimately connected with this quantum critical CO state.

Although the proposed picture provides a plausible resolution to the observed discrepancy between the temperature dependence of the RIXS phonon softening and the CO parameter, the spectroscopic traces are indirect, effectively scrambled by the Fano physics. We leave it as a challenge for other forms of spectroscopy to obtain a clearer view of this spectrum. Spectroscopies that can observe more directly CO fluctuations in a large momentum and energy regime can help to further refine the picture of dissipative CO quantum criticality by a metallic heat bath.

Online content

Any methods, additional references, Nature Research reporting summaries, source data, extended data, supplementary information, acknowledgements, peer review information; details of author contributions and competing interests; and statements of data and code availability are available at https://doi.org/10.1038/s41567-020-0993-7.

References

1. Keimer, B. et al. From quantum matter to high-temperature superconductivity in copper. *Nature* **518**, 179–186 (2015).
2. Varma, C. M. Pseudogap phase and the quantum-critical point in copper-oxide metals. *Phys. Rev. Lett.* **83**, 3538–3541 (1999).
3. Sachdev, S. Where is the quantum critical point in the cuprate superconductors? *Phys. Status Solidi B* **247**, 537–543 (2010).
4. Zaanen, J. Why the temperature is high. *Nature* **430**, 512–513 (2004).
5. Tranquada, J. M., Sternlieb, B. J., Axe, J. D., Nakamura, Y. & Uchida, S. Evidence for stripe correlations of spins and holes in copper oxide superconductors. *Nature* **375**, 561–563 (1995).
6. Howald, C., Eisaki, H., Kaneko, N. & Kapitulnik, A. Coexistence of periodic modulation of quasiparticle states and superconductivity in $Bi_2Sr_2CaCu_2O_{8+\delta}$. *Proc. Natl Acad. Sci. USA* **100**, 9705–9709 (2003).
7. Abbamonte, P. et al. Spatially modulated 'Mottness' in $La_{2-x}Ba_xCuO_4$. *Nat. Phys.* **1**, 155–158 (2005).
8. Ghiringhelli, G. et al. Long-range incommensurate charge fluctuations in (Y,Nd)$Ba_2Cu_3O_{6+x}$. *Science* **337**, 821–825 (2012).
9. Chang, J. et al. Direct observation of competition between superconductivity and charge density wave order in $YBa_2Cu_3O_{6.67}$. *Nat. Phys.* **8**, 871–876 (2012).
10. Comin, R. et al. Charge order driven by fermi-arc instability in $Bi_2Sr_{2-x}La_xCuO_{6+\delta}$. *Science* **343**, 390–392 (2014).
11. da Silva Neto, E. H. et al. Ubiquitous interplay between charge ordering and high-temperature superconductivity in cuprates. *Science* **343**, 393–396 (2014).
12. Tabis, W. et al. Charge order and its connection with Fermi-liquid charge transport in a pristine high-T_c cuprate. *Nat. Commun.* **5**, 5875 (2014).
13. Croft, T. P. et al. Charge density wave fluctuations in $La_{2-x}Sr_xCuO_4$ and their competition with superconductivity. *Phys. Rev. B* **89**, 224513 (2014).
14. Wen, J.-J. et al. Observation of two types of charge density wave orders in superconducting $La_{2-x}Sr_xCuO_4$. *Nat. Commun.* **10**, 3269 (2019).
15. Forgan, F. M. et al. The microscopic structure of charge density wave in underdoped $YBa_2Cu_3O_{6.54}$ revealed by X-ray diffraction. *Nat. Commun.* **6**, 10064 (2015).
16. Chaix, L. et al. Dispersive charge density wave excitations in $Bi_2Sr_2CaCu_2O_{8+\delta}$. *Nat. Phys.* **13**, 952–956 (2017).
17. Reznik, D. Phonon anomalies and dynamic stripes. *Physica C* **481**, 75–92 (2012).
18. Pintschovius, L. & Braden, M. Anomalous dispersion of LO phonons in $La_{1.85}Sr_{0.15}CuO_4$. *Phys. Rev. B* **60**, R15039–R15042 (1999).
19. Park, S. R. et al. Evidence for a charge collective mode associated with superconductivity in copper oxides from neutron and x-ray scattering measurements of $La_{2-x}Sr_xCuO_4$. *Phys. Rev. B* **89**, 020506(R) (2014).
20. Devereaux, T. P. et al. Directly characterizing the relative strength and momentum dependence of electron–phonon coupling using resonant inelastic x-ray scattering. *Phys. Rev. X* **6**, 041019 (2016).
21. Hashimoto, M., Vishik, I. M., He, R. H., Devereaux, T. P. & Shen, Z. X. Energy gaps in high-transition-temperature cuprate superconductors. *Nat. Phys.* **10**, 483–495 (2014).
22. Allen, P. B. et al. Neutron-scattering profile of $Q \neq 0$ phonons in BCS superconductors. *Phys. Rev. B* **56**, 5552–5558 (1997).
23. Le Tacon, M. et al. Giant phonon anomalies and central peak due to charge density wave formation in $YBa_2Cu_3O_{6.6}$. *Nat. Phys.* **10**, 52–58 (2014).
24. Kim, H. H. et al. Uniaxial pressure control of competing orders in a high-temperature superconductor. *Science* **362**, 1040–1044 (2018).
25. Sachdev, S. *Quantum Phase Transition* (Cambridge University Press, 2011).
26. Vojta, M. Lattice symmetry breaking in cuprate superconductors: stripes, nematics, and superconductivity. *Adv. Phys.* **58**, 699–820 (2009).
27. Kivelson, S. A. et al. How to detect fluctuating stripes in the high-temperature superconductors. *Rev. Mod. Phys.* **75**, 1201–1241 (2003).
28. Schmid, A. Diffusion and localization in a dissipative quantum system. *Phys. Rev. Lett.* **51**, 1506–1509 (1983).
29. Caldeira, A. O. & Leggett, A. J. Quantum tunnelling in a dissipative system. *Ann. Phys.* **149**, 374–456 (1983).
30. Sperstad, I. B., Stiansen, E. B. & Sudbo, A. Quantum criticality in spin chain with non-Ohmic dissipation. *Phys. Rev. B* **85**, 214302 (2012).
31. Peng, Y. Y. et al. Re-entrant charge order in overdoped $(Bi,Pb)_{2.12}Sr_{1.88}CuO_{6+\delta}$ outside the pseudogap regime. *Nat. Mater.* **17**, 697–702 (2018).
32. Miao, H. et al. Formation of incommensurate charge density wave in cuprates. *Phys. Rev. X* **9**, 031042 (2019).
33. Mitrano, M. et al. Ultrafast time-resolved x-ray scattering reveals diffusive charge order dynamics in $La_{2-x}Ba_xCuO_4$. *Sci. Adv.* **5**, eaax3346 (2019).
34. Arpaia, R. et al. Dynamical charge density fluctuations pervading the phase diagram of a Cu-based high- superconductor. *Science* **365**, 906–910 (2019).

Methods

Materials. High-quality Bi-2212 ($Bi_{1.7}Pb_{0.4}Sr_{1.7}CaCu_2O_{8+\delta}$) single crystals were grown by floating-zone methods. The crystals were annealed in nitrogen atmosphere to achieve a nearly optimally doped hole concentration with $T_C = 90\,K$; this corresponds to a doping concentration of ~13% holes per Cu cation. Flat crystals with a sharp Laue pattern were selected for the reported RIXS experiments.

Ultrahigh-resolution RIXS measurements. The RIXS measurements were performed using the RIXS spectrometer at the I21 RIXS beamline of the Diamond Light Source in the United Kingdom. The RIXS spectra were taken with the photon energy of the incident X-rays tuned to the maximum of the absorption curve near the Cu L_3 edge (Extended Data Fig. 1a). The scattering geometry is sketched in Extended Data Fig. 1b. The data were collected with a linear vertical polarization (σ polarization) of the incident beam. The energy resolution was $\Delta E \approx 35\,meV$ (FWHM) at the Cu L_3 edge. The scattering angle of the spectrometer was set at $2\theta = 146°$. Since the electronic state in Bi-2212 is quasi-two-dimensional, that is, rather independent along the c axis, the data shown in this report are plotted as a function of $q_\parallel$, that is, the projection of $\mathbf{q} = \mathbf{k}_f - \mathbf{k}_i$ onto the CuO_2 plane. $\mathbf{k}_i$ and $\mathbf{k}_f$ represent the incident and scattering photon momenta. Different $q_\parallel$ (projections of the scattering vector $\mathbf{q}$ along [100]) were obtained by rotating the samples around the vertical b axis. Note that the scattering vector $\mathbf{q}$ is denoted using the pseudotetragonal unit cell with $a = b = 3.82\,Å$ and $c = 30.84\,Å$, where the c axis is normal to the sample surface. In our convention, positive $q_\parallel$ corresponds to grazing-emission geometry and negative $q_\parallel$ corresponds to grazing-incidence geometry. For all RIXS data the $q_\parallel$ resolution is smaller than 0.02 r.l.u.

Data analysis and fitting. The data were normalized to incident photon flux and corrected for self-absorption effects using the formalism described in the Supplemental Material of ref. [35]. The zero-energy positions were determined by comparing the spectrum recorded from a small amount of silver paint (at each $q_\parallel$) near the sample surface, and fine tuned using the fitted elastic peak position, as shown in Extended Data Fig. 2a. The fitting model involves a Gaussian (elastic peak), an anti-Lorentzian (phonon peak) and a background using the tail of an antisymmetrized Lorentzian. The model is convolved with the energy resolution of the RIXS instrument (FWHM = 35 meV, Gaussian convolution) and fitted to the data. The results of these fits are presented in Extended Data Fig. 2b.

From this fitting analysis, we extracted the dispersion (peak positions) of the RIXS phonon shown in Fig. 2b. In addition, we also obtained the quasielastic maps in Fig. 1b,c and phonon maps in Fig. 2d by respectively subtracting the fitted phonon and elastic peaks from the raw data.

The CO peak profiles shown in Fig. 1e were fitted to a Gaussian peak with a linear background. For $T = 130$-K and 220-K data, the linear background is estimated by linear interpolation between the 90-K and 260-K data. The error bars of 130-K and 220-K data were estimated by the difference of the fitted parameter value using $T = 90$-K and 260-K background, respectively.

Model simulation of Fano effect between CO excitations and the bond-stretching phonons. An explicit calculation for the RIXS spectral function involves a four-particle correlation function, with an accurate description of the quantum critical charge-ordered state for the cuprates. Since such a description is not currently available, we instead appeal to general phenomenology and model the RIXS spectra as having a Fano lineshape, whereby the phonon seen in RIXS interacts with a charged particle continuum, that is CO collective modes. The Fano spectra were modelled using the form of the Raman response[36] with a straightforward generalization to finite q by using momentum-dependent electronic susceptibility (for CO excitations), phonon dispersion and electron–phonon coupling:

$$\chi''_{Fano}(\mathbf{q}, \omega) = \frac{(\omega + \omega_a(\mathbf{q}))^2}{\left(\omega^2 - \hat{\omega}_\lambda(\mathbf{q},\omega)^2\right)^2 + [2\omega_\lambda(\mathbf{q})\Gamma_\lambda(\mathbf{q},\omega)]^2}$$
$$\times \left\{ \gamma_\lambda^2 \chi''_\lambda(\mathbf{q}, \omega) \left[(\omega - \omega_a(\mathbf{q}))^2 + 4\Gamma_\lambda^i \Gamma_\lambda(\mathbf{q}, \omega) \left(\frac{\omega_\lambda(\mathbf{q})}{(\omega + \omega_a(\mathbf{q}))} \right)^2 \right] \right.$$
$$\left. + 4g_{PP}(\mathbf{q})^2 \Gamma_\lambda^i \left(\frac{\omega_\lambda(\mathbf{q})}{(\omega + \omega_a(\mathbf{q}))} \right)^2 \left[1 + \frac{\lambda(\mathbf{q},\omega)}{\beta(\mathbf{q})} \right]^2 \right\}$$

$\omega_a(\mathbf{q}) = \omega_\lambda(\mathbf{q}) \sqrt{1 + \beta(\mathbf{q})}$ sets the position of the antiresonance of the lineshape with $\beta(\mathbf{q}) = \frac{2g_{PP}g_\lambda(\mathbf{q})}{\Gamma_\lambda^i g_\lambda(\mathbf{q})}$, where $g_\lambda(\mathbf{q})$ is the electron–phonon coupling vertex, $\omega_\lambda(\mathbf{q})$ is the bare phonon frequency and γ_λ is a symmetry element of the Raman vertex projected out by the incoming and outgoing photon polarization vectors. For simplicity, we use the full charge vertex and set γ_λ to 1. $\chi_\lambda(\mathbf{q},\omega)$ is the momentum-dependent complex electronic susceptibility representing the CO excitations that causes the Fano effect on the phonon spectrum, whose real and imaginary parts are denoted as $\chi'_\lambda(\mathbf{q},\omega)$ and $\chi''_\lambda(\mathbf{q},\omega)$, respectively.

The renormalized phonon frequency is defined through the following equation: $\hat{\omega}_\lambda(\mathbf{q},\omega)^2 = \omega_\lambda(\mathbf{q})^2 (1 - \lambda(\mathbf{q},\omega))$, where $\lambda(\mathbf{q},\omega) = 2g_\lambda(\mathbf{q})^2 \chi'_\lambda(\mathbf{q},\omega)/\omega_\lambda(\mathbf{q})$. Γ_λ is the renormalized linewidth of the phonon, $\Gamma_\lambda(\mathbf{q},\omega) = \Gamma_\lambda^i + g_\lambda(\mathbf{q})^2 \chi''_\lambda(\mathbf{q},\omega)/\omega_\lambda(\mathbf{q})$, where Γ_λ^i is the intrinsic damping of the phonon away from $\mathbf{Q}_{CO}$. Finally, $g_{PP}(\mathbf{q})$ represents the photon–phonon coupling, which in principle is derivable from the direct resonant matrix elements[20].

Many of the parameters can be well constrained by the data. For example, the renormalized phonon frequency and linewidth can be obtained from the energy and momentum position of the phonon intensity near $\mathbf{Q}_{CO}$, while the bare phonon parameters can be obtained away from $\mathbf{Q}_{CO}$. The electronic response $\chi_\lambda(\mathbf{q},\omega)$ is determined by the response at low energies near $\mathbf{Q}_{CO}$, given the parameters of the CO collective modes. Finally, $g_{PP}(\mathbf{q})$ sets the overall intensity of the phonon relative to the continuum and $\beta(\mathbf{q})$ sets the position of the antiresonance (depletion of spectral weight) on the high-energy side of the phonon.

In this calculation, the momentum-dependent electron–bond-stretching phonon coupling takes the expected form $g_\lambda(\mathbf{q}) = g_{gg} \sin\left(\frac{\pi q}{2}\right)$ for deformational coupling with $g_{gg} = 0.123$. Constrained by the bond-stretching phonon energies at small $\mathbf{q}$ and near the zone boundary, we model the phonon dispersion $\omega_\lambda(\mathbf{q}) = 0.08 - 0.014 \sin\left(\frac{\pi q}{2}\right)$ in units of electron volts. The intrinsic phonon bandwidth Γ_λ^i is set to 0.005 eV. $g_{PP}(\mathbf{q})$ is expected to have the same functional form as $g_\lambda(\mathbf{q})$, thus, $g_{PP}(\mathbf{q}) = \mathbf{g}_{PP} \sin\left(\frac{\pi q}{2}\right)$ with $g_{PP} = 0.475$. Taking the simplest form for the electronic susceptibility of CO excitations, we assume $\chi_\lambda(\mathbf{q},\omega) = \frac{1}{\omega - \Omega_\mathbf{q}(\mathbf{q}) + i\Gamma(T)} - \frac{1}{\omega + \Omega_\mathbf{q}(\mathbf{q}) + i\Gamma(T)}$. The $\chi_\lambda(\mathbf{q},\omega)$ should also be multiplied by a density-of-states factor, which we assumed is a constant, and found that a value of 0.14 yields good agreement with our data. We use $\mathbf{c} = \sqrt{0.4}\,eV\,\pi$, with good agreement with the data. In addition, to account for the finite correlation length of CO, we also apply a Gaussian broadening on $\chi_\lambda(\mathbf{q},\omega)$ with FWHM corresponding to the CO width (Fig. 1e) to obtain the continuum of the CO quantum fluctuations (Fig. 1b). To determine $\Gamma(T)$, we fit the peak positions of the Fano spectrum near $\mathbf{Q}_{CO}$ to those in the data shown in Fig. 2b, while fixing other parameters.

Data availability

All other data that support the plots within this paper and other findings of this study are available from the corresponding author upon reasonable request.

References

35. Minola, M. et al. Collective nature of spin excitations in superconducting cuprates probed by resonant inelastic X-ray scattering. *Phys. Rev. Lett.* **114**, 217003 (2015).
36. Devereaux, T. P., Virosztek, A. & Zawadowski, A. Charge-transfer fluctuation, d-wave superconductivity, and the B1g Raman phonon in cuprates. *Phys. Rev. B* **51**, 505–514 (1995).

Acknowledgements

Author contributions

W.S.L. conceived the experiment. W.S.L., K.-J.Z., M. Hepting, J.L., A.N., A.C.W., M.G.-F. and H.R. conducted the experiment at the Diamond Light Source. J.L., A.N. and K.-J.Z. performed the data processing from the detector. W.S.L., M. Hepting and H.L. analysed the data. W.S.L., B.M., J.Z. and T.P.D. performed the theoretical calculations. K.-J.Z., A.C.W. and M.G.-F. constructed and commissioned the ID21 RIXS beamline and spectrometer at the Diamond Light Source. M. Hashimoto, D.S. and H.E. synthesized and prepared samples for the experiments. W.S.L., Z.X.S., B.M., J.Z. and T.P.D. wrote the manuscript with input from all authors.

Competing interests

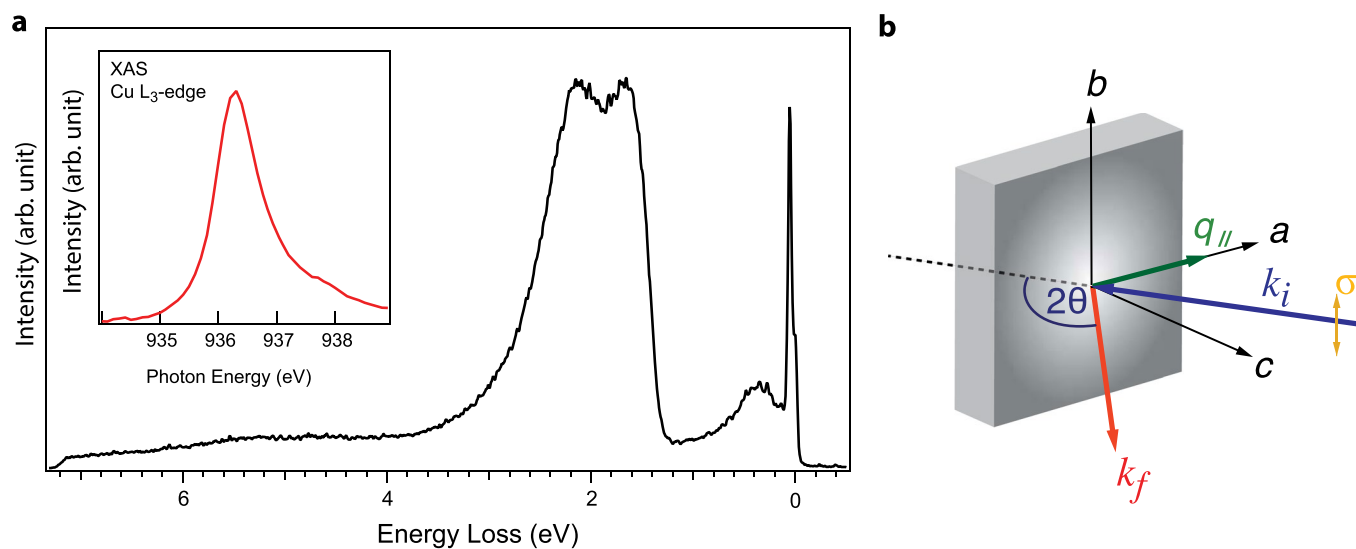The authors declare no competing interests.

Additional information

a

b

Extended Data Fig. 1 | RIXS experiment and scattering geometry. a, A representative RIXS spectral taking at Cu L_3-edge. In this work, we discuss the inelastic scattering signal below 0.1 eV. The inset shows a typical x-ray absorption curve across the Cu L_3-edge, taken by measuring total florescent yield. **b**, A sketch of the scattering geometry. The crystal axes are denoted as a, b and c. k_i and k_f represent the incident and scattering photon momentum. 2θ is the scattering angle. The yellow arrow represents the polarization of the incident x-ray. All the data shown in this manuscript were taken using incident beam with sigma polarization.
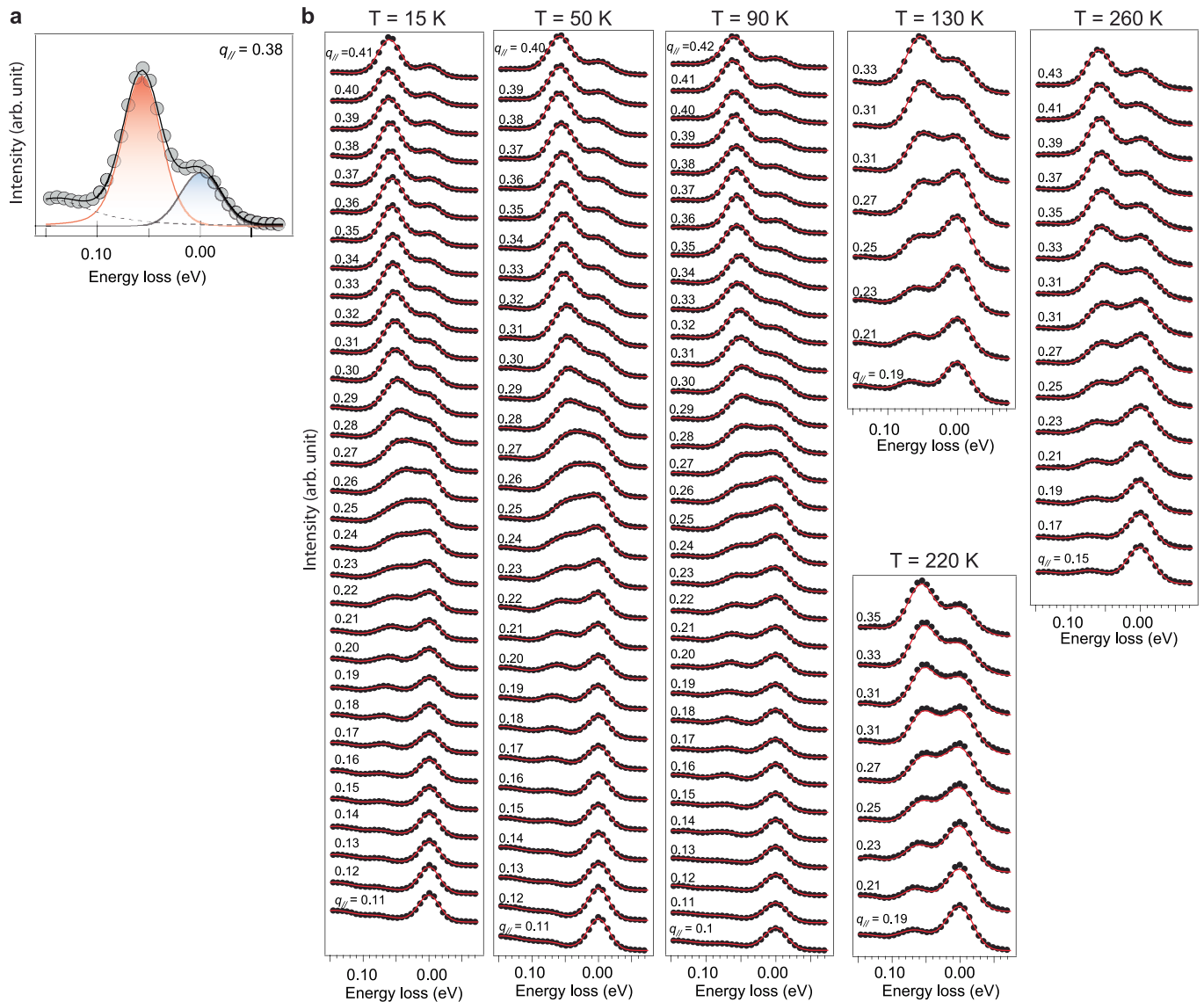
Extended Data Fig. 2 | Raw RIXS spectra and Fitting. a, An example of the spectra fitting. The fit function consists of a Gaussian function for the elastic peak (blue), an anti-Lorentzian function for the RIXS phonon (red), and a smooth background from high energy (black dashed line). The fit function is convoluted with a Gaussian function with a FWHM corresponding to the energy resolution of the RIXS instrument and fit to the data. **b**, All Raw RIXS spectra discussed in this work. The red curves are the fits, showing good agreements with the experimental data.
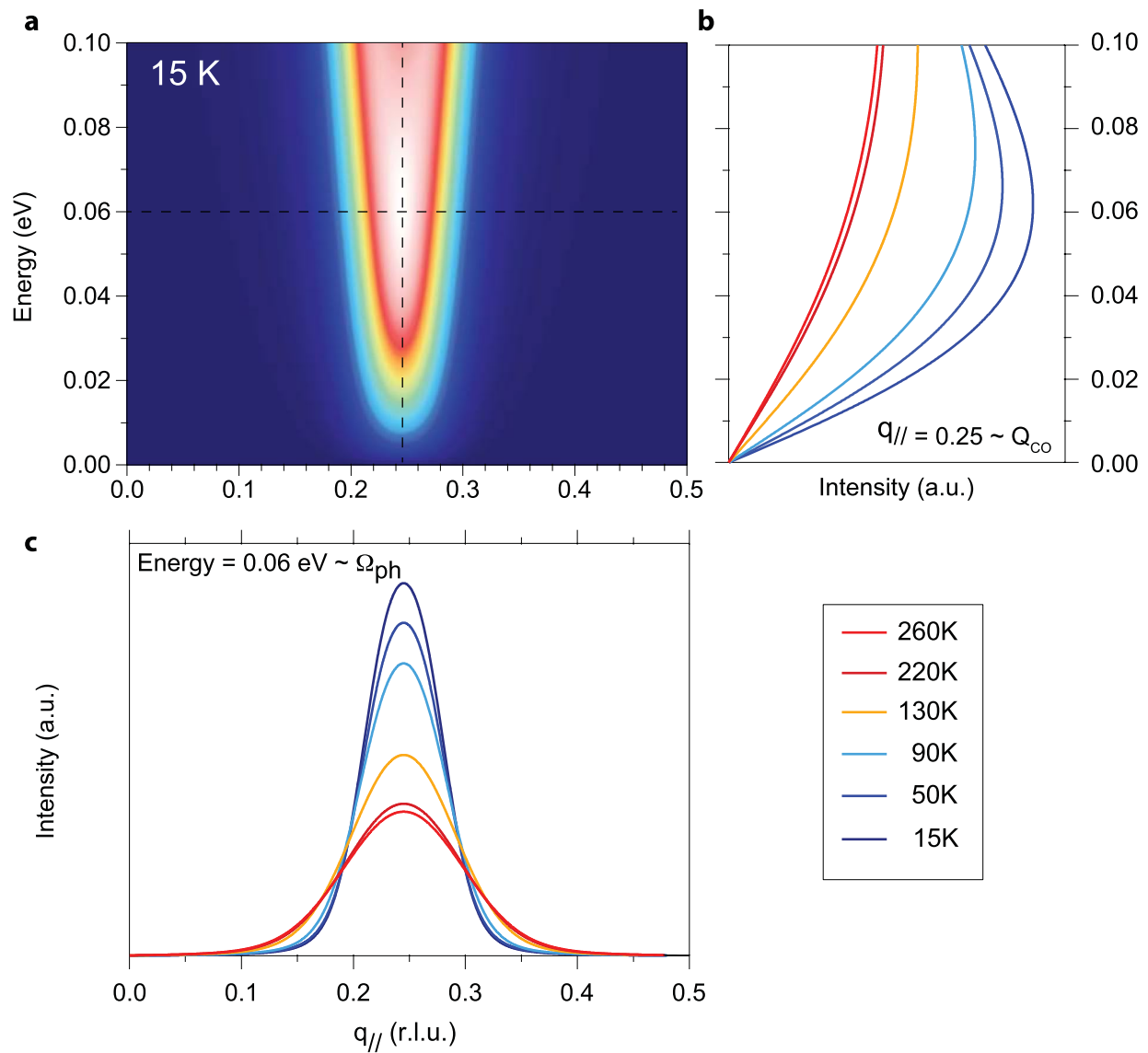
Extended Data Fig. 3 | CO excitations continuum used in the model. a, Intensity map of $Im[\chi_\lambda(\mathbf{q},\omega)]$ with for modeling 15 K data. **b**, Energy distribution curves at Q_{CO} (the vertical black dashed lines in **a**) with different values of the damping Γ that are used to model the temperature dependence behavior shown in Fig. 4c. **c**, Momentum distribution curve at 0.06 eV (the horizontal black dashed lines in **a**), approximately at the bond-stretching phonon energy.